Analytical Methods

ROYAL SOCIETY OF CHEMISTRY

PAPER

View Article Online
View Journal

Cite this: DOI: 10.1039/d6ay00164e

Development and validation of a cross-species breath metabolomics platform for translational VOC analysis

Zhiheng Yu, Yongyan Ji, Zijun Meng and Xiang Li *

The lack of universal cross-species sampling and quality control methods has limited the potential of breath metabolomics to advance from clinical discovery to mechanistic validation. To address this challenge, this study developed and systematically validated an integrated cross-species breath analysis platform, with its core components comprising a high-sensitivity mouse breath sampling system (FaunaScope) and a quality control (QC) strategy incorporating behavioral monitoring. By identifying ethyl acetate and dimethyl sulfide as characteristic interference markers, the platform exhibited high detection capability and good analytical reproducibility in the analysis of 33 core volatile organic compounds (VOCs) in mouse breath, with detection rates exceeding 88.2% for 30 VOCs and coefficients of variation below 30% for more than 70% of the compounds. Using inflammatory bowel disease (IBD) as a demonstration model, the platform enabled a full-chain study from validation of breath fingerprints in clinical patients to longitudinal monitoring in mouse models, successfully capturing dynamic metabolic changes in short-chain fatty acids (SCFAs) and responses to exclusive enteral nutrition (EEN) intervention, while revealing metabolic feature divergence between humans and mice attributable to differences in pathological mechanisms. Overall, this platform exhibits high sensitivity and strong resistance to interference, providing an effective translational medicine tool for linking clinical findings with fundamental mechanistic research.

Received 28th January 2026
Accepted 23rd April 2026

DOI: 10.1039/d6ay00164e

rsc.li/methods

1 Introduction

Breath metabolomics, as an emerging non-invasive analytical technique, captures volatile organic compounds (VOCs) from metabolism in exhaled breath. It can reflect pathophysiological states in real time and shows great potential for screening and monitoring various diseases. For example, specific breath biomarkers have been successfully identified for the perioperative monitoring of lung cancer.[1] In the field of digestive system tumors, an AI-enhanced breath volatilomics platform was pioneered for efficient, non-invasive early screening of colorectal cancer.[2] However, despite these advances, the clinical translation of breath biomarkers is often limited by inherent confounding factors in human studies, such as diet, environmental exposure, and medication. These factors obscure the true biological origin of the detected VOCs. To address this challenge, animal models, especially mouse models, have become ideal tools for elucidating the generation mechanisms of biomarkers. This is due to their advantages of a controllable environment and the ease of invasive pathological validation. In recent years, several studies have successfully collected and identified disease-specific breath fingerprints in mouse models. Typical examples include identifying infection-related VOCs in *Pseudomonas aeruginosa* infections and distinguishing tuberculosis-like infections from control groups through breath screening.[3,4] Additionally, a systematic review has summarized and evaluated the methodologies and findings in animal breath research,[5] proving the feasibility and value of animal breath studies in mechanism elucidation and biomarker validation.

However, to advance breath analysis from clinical observation to pathological mechanism elucidation, translational research still faces severe technical barriers. First, in terms of sampling strategies, although sampling bags (*e.g.*, Tedlar bags) are widely used in clinical and animal studies due to their convenience,[3,6–10] their limitations in sensitivity, temporal resolution, and background contamination control are becoming apparent. Studies have shown that polymer bags can compromise sample integrity through analyte adsorption loss or material background outgassing, which is particularly detrimental to the analysis of trace VOCs.[11,12] Second, regarding detection techniques, while online mass spectrometry (*e.g.*, PTR-MS and SIFT-MS) has been used in numerous studies for large-scale disease screening and characterization due to its real-time monitoring advantage,[13,14] it has limitations. As highlighted in authoritative reviews, online mass spectrometry techniques lack separation steps like chromatography. This results in significant limitations in resolving isomers and in the structural identification of new compounds, thereby limiting

Shanghai Key Laboratory of Air Quality and Environmental Health, Department of Environmental Science & Engineering, Fudan University, Shanghai 200438, P.R. China. E-mail: lixiang@fudan.edu.cn

their potential application in the in-depth tracing of complex metabolic pathways.[15] In contrast, offline analysis based on gas chromatography-mass spectrometry (GC-MS) provides higher structural resolution. Numerous studies have confirmed its gold-standard status in the discovery of novel biomarkers and in full-spectrum metabolomic analysis.[16–18] However, this technique demands extremely high enrichment efficiency and cleanliness from the sampling front-end.[19] Critically, existing breath sampling devices designed for laboratory animals still have design flaws. Intubation-based ventilation systems can reduce ambient air contamination, but the procedure is invasive and introduces system background from complex tubing.[20] In contrast, non-invasive whole-body or nose-only exposure chambers, while avoiding anesthesia, are highly susceptible to contamination from non-respiratory sources (mainly excreta, *i.e.*, urine and feces).[21] Overall, these devices generally lack effective quality control (QC) mechanisms for the excretory behavior of rodents. The matrix effect from high-concentration VOCs released by excreta can easily mask trace endogenous breath signals. This leads to a significant decrease in the data's signal-to-noise ratio and reproducibility. This has become a key bottleneck that prevents current animal breath research from achieving reliable, high-fidelity correlation with high-quality clinical data.

To address the core analytical challenges in ensuring sampling reliability and controlling matrix interference, this study developed and systematically validated an integrated cross-species breath metabolomics research platform. At the platform's methodology level, we first focused on the bottleneck of sampling technology. We independently developed a high-performance breath collection system for small laboratory animals—the FaunaScope. This system employs a compact geometric design matched to the mouse's size, aiming to minimize dead volume. It is seamlessly integrated with high-sensitivity thermal desorption-gas chromatography-tandem mass spectrometry (TD-GC-MS/MS). Critically, to address the interference from complex biological matrices at the source, we established a pioneering quality QC strategy. This strategy combines real-time behavioral monitoring with the identification of interference biomarkers characteristic of excretion, ensuring the collection of high-fidelity pure breath samples. To rigorously test and demonstrate the platform's performance under complex pathophysiological conditions, we selected Inflammatory Bowel Disease (IBD) as a demanding demonstration model. The "gut–lung axis" metabolic feature of IBD, *i.e.*, metabolites such as short-chain fatty acids (SCFAs) produced by gut microbiota must cross a compromised intestinal barrier and be exhaled *via* blood circulation,[22] is a weak and complex signal transduction process that poses a great challenge to the analytical platform's sensitivity and anti-interference capability. In this study, the platform was not only successfully applied to the longitudinal monitoring of a dextran sulfate sodium (DSS)-induced colitis mouse model and its response to exclusive enteral nutrition (EEN) intervention, but more importantly, it accurately captured the phenomenon of metabolic feature divergence between humans and mice caused by the pathological differences between "acute gut leakage" and "chronic dysregulation". This result highlights the excellent capability of this platform in detecting subtle metabolic fluctuations within complex biological matrices. Therefore, this study establishes a reliable analytical tool for translational research, capable of providing a solid bridge to connect clinical phenotypes with their underlying pathobiological mechanisms.

2 Experimental

2.1 Overview of the breath analysis platform

This study constructed an integrated cross-species breath metabolomics research platform. It aims to break the barrier between clinical phenomena and basic mechanisms to achieve a closed loop in translational medicine research. The platform is based on the human breath analysis technology previously established by our team.[23] It was extended by integrating a self-developed breath collection system for small laboratory animals (FaunaScope). This provides the capability for cross-species analysis of breath VOCs.

As shown in Fig. 1A, the platform architecture covers two parallel routes: (1) a clinical discovery route, which supports non-invasive breath sampling and high-throughput biomarker screening based on large-scale human cohorts; (2) a basic validation route, which utilizes the FaunaScope breath collection system for long-term, non-invasive breath monitoring and mechanism elucidation in various small laboratory animal models. Both routes rely on a unified high-sensitivity detection core—the thermal desorption-gas chromatography-tandem mass spectrometry (TD-GC-MS/MS) system. This is combined with automated data preprocessing and multivariate statistical analysis to ensure high fidelity and comparability of cross-species data.

2.2 Human study cohort and breath sample collection

The clinical cohort and breath sample repository used in this study were derived from breath sample resources previously established and reported by our group. Based on this cohort, our prior work has preliminarily revealed associations between breath metabolic profiles and the gut microbiota in patients with IBD.[24] Building upon these findings, the present study extended the research scope beyond descriptive correlation analyses and instead focused on the entire workflow of breath-based investigations, with the aim of systematically constructing an integrated translational breath analysis platform. All experiments were performed in compliance with relevant laws and institutional guidelines. The study protocol was approved by the Ethics Committee of the affiliated hospitals of Fudan University (Approval No. FE22139I), and informed consent was obtained from all human subjects prior to their participation in the study. Participant recruitment followed the STARD guidelines. Patients in the IBD group were diagnosed based on a comprehensive assessment of clinical manifestations, endoscopic findings, and histopathology, while healthy controls (HCs) were recruited from individuals undergoing routine health examinations during the same period and without

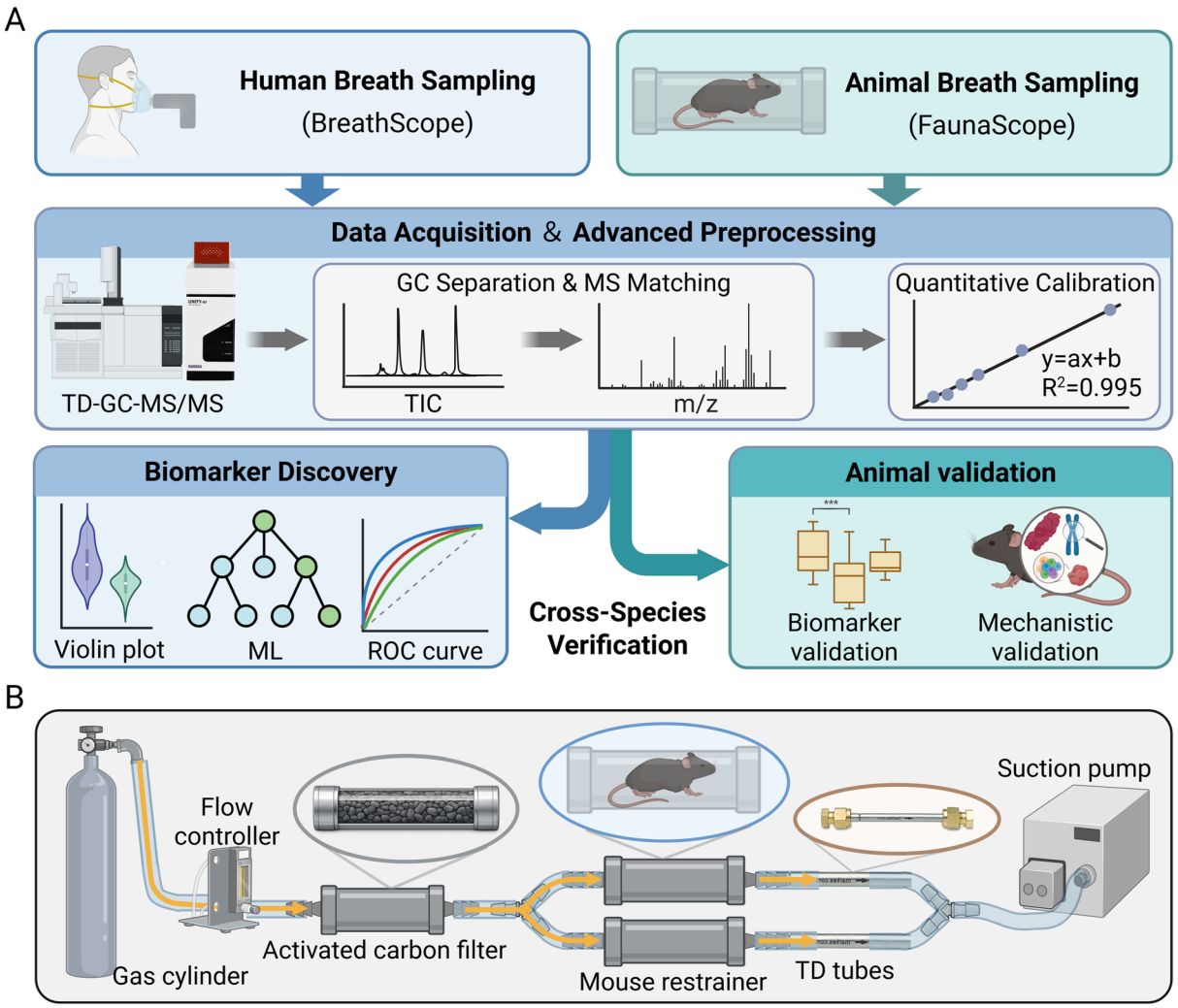

Fig. 1 An integrated platform for standardized cross-species breath analysis. (A) Workflow of the integrated platform, integrating parallel breath sampling from humans (BreathScope) and mice (FaunaScope) with a unified TD-GC-MS/MS analytical pipeline for biomarker discovery and validation. (B) Schematic of the FaunaScope system for non-invasive mouse breath collection.

gastrointestinal or systemic diseases. To minimize potential confounding factors, strict inclusion and exclusion criteria were applied, as detailed in the SI (Text S1).

Breath sample collection was performed according to a Standard Operating Procedure (SOP). All participants were required to fast overnight (>8 h) and underwent sampling between 07:00 and 09:00 in the morning. Prior to sampling, subjects were instructed to rinse their mouths and avoid strenuous physical activity to reduce exogenous interference. Breath sampling was conducted using a ReCIVA™ breath sampler (Owlstone Medical, UK), coupled with a CASPER clean air supply unit, and preferential collection of the alveolar fraction was achieved under temperature-controlled conditions. Exhaled breath was enriched onto sorbent tubes (Tenax TA/Carbograph 5TD) at a flow rate of 200 mL min^{-1}, with a total collection volume of 2.0 L per sampling session. Urine samples collected synchronously with breath sampling and their corresponding processing procedures are described in the SI (Text S2).

2.3 Design and working principle of the breath collection system for small laboratory animals

To address the problems of sample dilution and background interference in traditional animal breath collection, this study developed a dual-channel breath collection system for small laboratory animals (FaunaScope, Fig. 1B). The device mainly consists of three parts: a gas supply, an animal restrainer, and an adsorption trapping unit.

At the gas supply end, high-purity synthetic air (air, 99.999%) serves as the carrier gas. Its flow rate is precisely controlled by a mass flow controller before it passes through an activated charcoal adsorption filter. This step is designed to remove trace organic impurities from the gas source and tubing. This establishes a low background sampling baseline, ensuring that detected VOCs originate from the experimental animal and not from environmental interference.

The core sampling component is a custom-made transparent polymethyl methacrylate (PMMA) restrainer. Its transparent

material allows for real-time observation of the mouse's state. Its compact internal structure is designed to reduce dead volume, thereby effectively minimizing the dilution of the breath sample by the carrier gas. To ensure the fidelity of sample transfer, all connecting tubes and fittings within the device are made of polytetrafluoroethylene (PTFE). This material has an extremely low chemical background and adsorptivity, which minimizes the contamination or loss of VOCs in the tubing.

The device employs a dual-channel parallel design, allowing for the independent sampling of two small laboratory animals simultaneously. Driven by the negative pressure of a mini vacuum pump, the purified carrier gas continuously flows through the restrainer. It carries the metabolic gases exhaled by the animal through a thermal desorption tube (TD tube) at a constant flow rate, achieving online enrichment and collection of breath VOCs.

2.4 Experimental animals and IBD modeling and intervention

Six-week-old male C57BL/6 mice were used in this study and were obtained from Shanghai SLAC Laboratory Animal Co., Ltd. All experimental procedures were approved by the Ethics Committee for Experimental Animals of Fudan University (Approval No. 2022JS Public Health-004). Detailed housing and husbandry conditions are provided in the SI (Text S3).

To minimize potential interference of stress induced by restraint and handling on breath metabolic profiles, a 3-day acclimation period (Days 1–3) was implemented prior to the formal experiments. During this period, all mice underwent standardized device acclimation training to gradually familiarize them with the breath sampling environment (detailed procedures are described in SI, Text S3). From Day 4 onward, mice were randomly assigned to a DSS-induced group or an EEN intervention group ($n = 6$ per group). In both groups, acute colitis was induced by providing ad libitum access to a 2% (w/v) DSS solution (molecular weight 36 000–50 000; MP Biomedicals, LLC., USA) for 8 consecutive days. During the modeling period, mice in the EEN group received exclusive enteral nutrition formula (4.5 g/18 mL) in place of standard chow to mimic a clinical nutritional intervention regimen.

Throughout the modeling period, clinical symptoms were monitored daily and the disease activity index (DAI) was calculated. The DAI score was determined based on a composite assessment of body weight change, stool consistency, and the presence of fecal blood, with detailed scoring criteria provided in the SI (Table S1).

2.5 Sampling protocol and quality control

To improve inter-sample comparability and data stability, this study established a strict SOP. Before breath sampling, all mice underwent 12 hours of overnight fasting, and the procedure was completed within the same time window (08:00–12:00). At the start of sampling, the restrained mice were pre-flushed for 5 minutes with clean air at a flow rate of 200 mL min^{-1}. This was done to remove residual background signals from the lungs and tubing and to establish a stable baseline. Subsequently, the sampling phase began. Based on the theoretical minute ventilation of C57BL/6 mice (approx. 60–70 mL min^{-1}),[21] the sampling flow rate was set consistent with the flushing phase. Sampling was performed continuously for 8 minutes, for a total breath volume exceeding 500 mL, thereby achieving sufficient enrichment of trace VOCs. After collection, all samples were immediately sealed and stored at 4 °C, and all subsequent analyses were completed within 24 hours.

Quality control was maintained throughout the entire sampling process. The core QC strategy involved real-time monitoring of excretion interference: any sample with a recorded defecation or urination event during sampling was labeled as a "contaminated sample (WE)" and was excluded from subsequent data analysis (see Section 3.4 for details). Furthermore, for each sampling batch, a gas sample from the unloaded device was collected concurrently as an environmental blank for background subtraction. All procedures were performed by the same trained operator to minimize systematic and human errors.

2.6 Instrumental analysis method

Sample analysis was performed using an automated thermal desorption system (Markes TD100-xr) coupled with a gas chromatography-triple quadrupole tandem mass spectrometer (Agilent 8890/7000D). The analytical procedure involved a two-stage thermal desorption pretreatment: the sorption tube was first dry-purged to remove moisture, then desorbed at 300 °C (first-stage desorption) and cryo-focused in a cold trap set at 30 °C. The cold trap was subsequently flash-heated to 300 °C at the maximum ramp rate (second-stage desorption), injecting the VOCs in splitless mode into the GC system. Chromatographic separation was carried out on a DB-624 capillary column (60 m × 0.25 mm × 1.4 μm), and mass spectrometric detection was operated in electron ionization (EI) mode.

Compound identification was based on matching full-scan data (m/z 30–350) against the NIST20 library. For quantitative analysis, a combined approach of Selected Ion Monitoring (SIM) and Multiple Reaction Monitoring (MRM) was employed, with precise quantification achieved by constructing standard curves using the external standard method. Specifically, standard calibration curves were constructed by injecting 1 μL of standard mixture solutions and internal standards into conditioned sorbent tubes, with each concentration level repeated in triplicate to mimic breath sampling. The calibration curves were established based on the peak area ratios (target analyte to internal standard) *versus* mass concentrations. The detailed concentration ranges, linear dynamic ranges, and correlation coefficients (R^2) for the targeted compounds are comprehensively summarized in SI Table S2. By acknowledging the inherent differences in the abundance of breath metabolites and sampling volumes between humans and mice (2.0 L *vs.* 0.5 L), species-specific targeted quantitative libraries were developed. For human samples, a target list comprising 71 VOCs was established (see SI Table S3 for details). For mouse samples, 33 core VOCs with high detection rates were selected for focused

Table 1 Baseline profile and analytical performance characteristics of 33 core VOCs identified in healthy mouse breath using the FaunaScope system (the unit "ng L^{-1}" refers to nanograms per liter of exhaled breath).

No.	Compound name	RT (min)	Mean ± SD (ng L^{-1})	CV (%)	LOD (ng L^{-1})	LOQ (ng L^{-1})	Detection rate (%)
1	Acetic acid	12.76	$(2.04 \pm 0.73)\times10^{3}$	35.73	40.080	94.295	100.0
2	Propionic acid	16.98	7.36 ± 3.14	22.70	0.068	0.159	100.0
3	Dimethyl sulfide	16.76	$(6.00 \pm 1.00)\times10^{-2}$	13.47	0.054	0.065	88.2
4	Isobutyric acid	18.88	1.09 ± 0.58	29.20	0.124	0.353	100.0
5	Butyric acid	19.92	2.66 ± 1.19	24.59	0.004	0.012	100.0
6	Valeric acid	23.88	0.94 ± 0.42	45.11	0.006	0.018	100.0
7	D-Limonene	27.28	2.40 ± 1.23	51.38	0.410	0.930	100.0
8	Benzonitrile	27.87	0.15 ± 0.03	18.13	0.107	0.219	100.0
9	Phenol	28.76	0.72 ± 0.25	34.45	0.201	0.342	100.0
10	Geranyl acetone	37.87	2.34 ± 0.84	35.78	0.087	0.225	100.0
11	Propionaldehyde	7.21	0.50 ± 0.12	23.30	0.713	1.365	11.8
12	Acetone	7.38	34.23 ± 11.58	33.82	2.858	8.373	100.0
13	Isopropanol	7.63	95.27 ± 66.53	69.83	0.561	1.324	100.0
14	Methacrolein	9.65	0.44 ± 0.33	73.52	0.460	0.814	47.1
15	Ethyl acetate	11.09	0.93 ± 0.56	59.91	0.332	0.732	100.0
16	Tert pentanol	12.90	0.26 ± 0.16	60.75	0.014	0.033	100.0
17	Butanol	14.04	1.22 ± 0.27	22.44	0.781	1.735	100.0
18	2-Pentanone	14.98	0.19 ± 0.02	12.48	0.222	0.414	35.3
19	Acetoin	16.76	5.51 ± 2.03	36.84	0.397	1.141	100.0
20	Hexanal	19.24	0.75 ± 0.12	15.34	0.246	0.317	100.0
21	1,2-Propanediol	19.28	0.40 ± 0.06	15.60	0.202	0.233	100.0
22	2-Heptanone	23.02	0.25 ± 0.06	23.88	0.156	0.161	100.0
23	Heptanal	23.32	0.65 ± 0.18	27.28	0.117	0.223	100.0
24	Benzaldehyde	26.53	1.04 ± 0.29	28.41	0.542	0.871	100.0
25	Octanal aldehyde	27.09	0.73 ± 0.19	25.82	0.167	0.330	100.0
26	Nonanal	30.20	1.69 ± 0.63	37.35	0.614	1.534	100.0
27	Decanal	32.64	0.49 ± 0.20	30.83	0.338	0.476	76.5
28	Decane	25.40	0.18 ± 0.07	41.79	0.151	0.304	58.8
29	Undecane	28.79	0.39 ± 0.23	60.53	1.392	3.830	5.9
30	Dodecane	31.42	0.45 ± 0.17	37.28	0.656	1.598	5.9
31	Tridecane	33.54	0.65 ± 0.19	29.55	0.243	0.482	100.0
32	Tetradecane	35.44	2.90 ± 0.93	32.03	0.556	1.088	100.0
33	Pentadecane	37.50	5.02 ± 0.87	17.38	0.723	1.590	88.2

monitoring (see Section 3.2, Table 1). The abbreviations and full names of these compounds are provided in Table S4 in the SI. Detailed parameters for the TD, the GC oven temperature program, and MS conditions can be found in the supplementary materials (Text S4).

2.7 Biological sample processing and histopathological assessment

At the experimental endpoint, mice were euthanized, and the entire colon, from the cecum to the anus, was dissected. The natural stretched length of the colon was measured and photographed, serving as a gross morphological indicator to assess the degree of inflammation. Subsequently, a segment of the distal colon (approximately 1 cm from the anus) was excised and fixed in 4% neutral-buffered paraformaldehyde at 4 °C for 24–48 hours. The fixed tissues were then embedded in paraffin, from which 4–5 μm serial sections were prepared and subjected to Hematoxylin and Eosin (H&E) staining.

Histopathological evaluation was conducted using a comprehensive scoring system (total score range: 0–15), with detailed criteria provided in the SI (Table S5). To eliminate subjective bias, the scoring was performed using a strict double-blind strategy. Two pathologists, unaware of the group assignments, independently evaluated the slides under 200× magnification. If the discrepancy between their scores was greater than 1 point, a third pathologist was brought in for a review. The final histological score for each sample, used in statistical analysis, was the average of the scores.

2.8 Data processing and multivariate statistical analysis

The raw GC-MS data were processed using the Agilent MassHunter Workstation for deconvolution, alignment, and internal standard normalization. The detailed preprocessing and machine learning analysis pipelines for both human and mouse data are described in the SI (Text S5). For the human data, a machine learning pipeline was constructed: after imputing missing values using Multivariate Imputation by Chained Equations (MICE), the dataset was randomly partitioned into a training set and a testing set at an 8 : 2 ratio using stratified sampling. To strictly prevent data leakage, feature standardization (Z-score) parameters were fitted exclusively on the training set. Inter-group differences were assessed using the Mann–Whitney U test combined with False Discovery Rate (FDR) correction ($p < 0.05$; FDR < 0.1). Multiple models,

including random forest and XGBoost, were deployed, and their diagnostic performance was evaluated using the ROC-AUC.

For the mouse data, the data underwent log 10 transformation and standardization before being subjected to Principal Component Analysis (PCA). Differences among multiple groups were analyzed using a one-way analysis of variance (ANOVA) followed by Tukey's HSD post-hoc test, with FDR correction (FDR < 0.1) also applied to control for false positives.

3 Results and discussion

3.1 Analytical performance evaluation of the FaunaScope system

To systematically evaluate the self-developed FaunaScope breath collection system, this study first analyzed breath samples from healthy C57BL/6 mice. Through collection with the FaunaScope and analysis by TD-GC-MS/MS, we robustly established a baseline mouse breath metabolic profile. It consists of 33 core VOCs (Table 1). This profile covers various chemical classes, including short-chain fatty acids (*e.g.*, acetic acid and propanoic acid), ketones, aldehydes, and alkanes. The method demonstrated excellent detection capability. 30 of the 33 target compounds (90.9%) achieved a high detection rate of over 88.2% across the entire animal cohort. 24 of these compounds (72.7%) were detected in 100% of the samples. This high detection coverage demonstrates that the FaunaScope system can efficiently capture trace metabolites. This provides a reliable basis for constructing representative breath fingerprints.

Further methodological validation assessed the sensitivity and precision of the analytical workflow (Table 1). The method exhibited extremely low limits of detection for various key metabolites, for example, propanoic acid (LOD: 0.068 ng L^{-1}) and butanoic acid (LOD: 0.004 ng L^{-1}), ensuring the accurate quantification of trace signal molecules. The low detection rate of some long-chain alkanes (*e.g.*, undecane and dodecane) (approx. 5.9%) can be attributed to their concentrations under healthy baseline conditions being far below their respective limits of detection. This precisely reflects the method's ability to objectively distinguish background noise from true biological signals. In terms of precision, the coefficients of variation (CVs) for all target analytes ranged from 12.48% to 73.52%. Notably, the CV values for over 70% (24/33) of the compounds, including various core metabolites such as propanoic acid (29.08%), butanoic acid (22.18%), and 1,2-propanediol (15.60%), were all below 30%. This indicates that the entire collection and analysis workflow possesses high robustness. For the few compounds with higher CV values, their variation is more likely to originate from the unavoidable inter-individual biological differences in living animals, rather than from the technical variation of the method itself.

To further demonstrate the analytical superiority of the FaunaScope, a comprehensive comparison with conventional sampling methods (*e.g.*, Tedlar bags and conventional animal exposure chambers) was conducted (see SI Table S6 for details). Conventional exposure chambers often involve relatively large internal volumes, which can introduce dilution effects and reduce the effective concentration of trace VOCs, thereby potentially decreasing signal-to-noise ratios.[21] Furthermore, Tedlar bags are known to emit interfering background VOCs such as phenol and *N*,*N*-dimethylacetamide.[8,25] The FaunaScope overcomes these limitations through its inert material composition and minimized dead volume, thereby significantly improving the signal-to-noise ratio for *in vivo* breath monitoring.

In summary, the FaunaScope system combined with TD-GC-MS/MS analysis constitutes a highly sensitive and precise analytical workflow. This workflow lays a solid analytical methodological foundation for reliably capturing and quantifying faint metabolic changes in complex disease models.

3.2 Extraction of metabolic features and analysis of translational challenges in a demonstrative clinical application

To establish a clinical reference for cross-species research and to explore methodological barriers in the translational process, we first used IBD as a demonstration model to conduct a full-spectrum analysis of breath VOCs on a clinical cohort containing 118 patients and 118 HC (Fig. 2A). The total ion chromatogram (TIC) intuitively revealed the systemic metabolic suppression triggered by the disease. The breath profile of IBD patients showed significant signal down-regulation in specific retention time windows (*e.g.*, 10–20 min) (Fig. 2B). This overall hypometabolic state may originate from the impaired anabolic function of the body or the excessive consumption of specific substrates in the disease state. Highly consistent with previous reports, multiple studies have confirmed the phenomenon of abundance down-regulation of specific metabolite clusters in the breath profiles of IBD patients.[26,27]

Based on the quantitative data of 71 core VOCs established by the methodology, this study further employed seven mainstream machine learning algorithms to build diagnostic models. Among them, the random forest (RF) model exhibited the optimal classification performance in test set validation (Fig. 2C). Its area under the ROC curve (AUC) reached 0.815 (Fig. 2D), significantly outperforming other models. The robustness of the RF model to class imbalance and feature collinearity in high-dimensional data processing is the key to its excellent diagnostic efficacy, and this advantage has also been confirmed in studies on complex disease biomarker screening.[28] To precisely identify the most biologically significant core biomarkers, we adopted a strict multi-step screening strategy: a compound had to simultaneously satisfy being in the top 15 for feature importance in the random forest model, showing significant inter-group differences (Mann–Whitney U test, $p < 0.05$, and FDR < 0.1) and having a clear gut microbial metabolic origin. Through this strategy, we ultimately identified 4 key biomarkers: propanoic acid, butanoic acid, isobutanoic acid, and 1,2-propanediol.

Compared to the healthy control group, the abundances of these four biomarkers in the breath of IBD patients were all drastically down-regulated (Fig. 2E). Specifically, the mean concentration of the core biomarker propanoic acid decreased

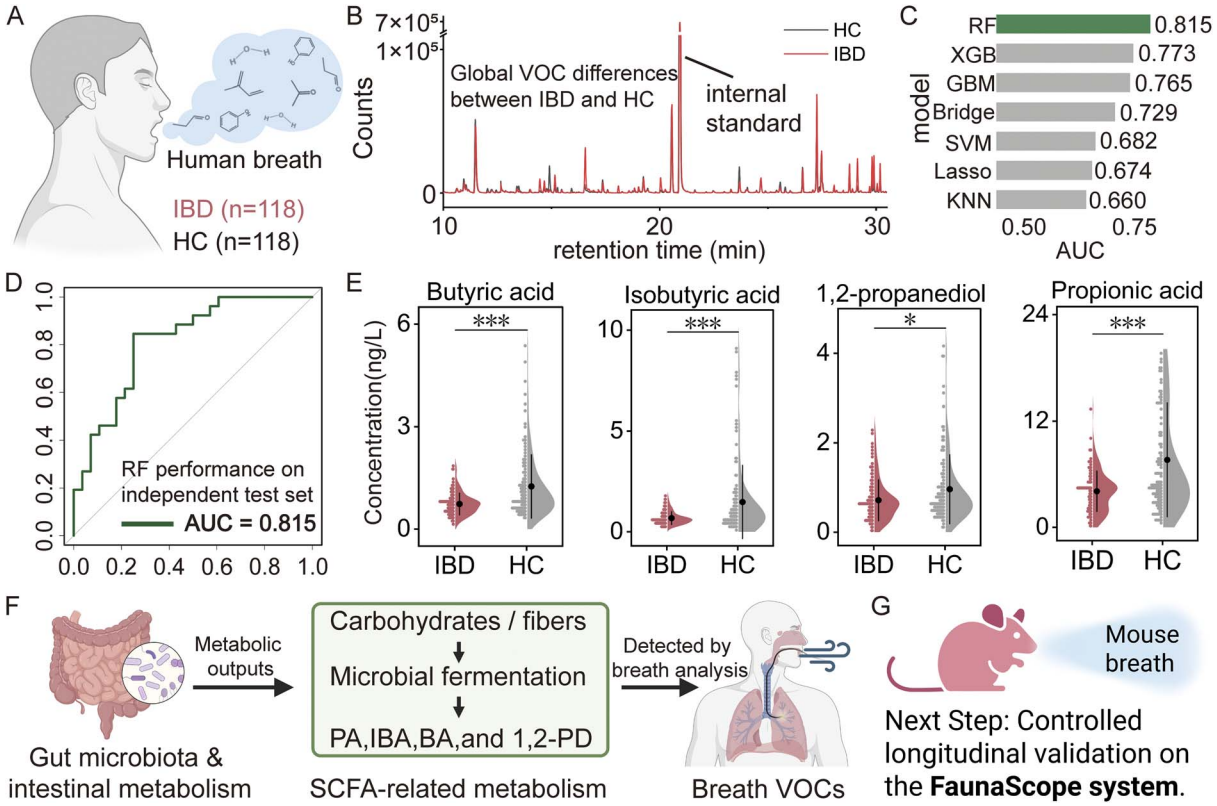

Fig. 2 Discovery of breath volatile biomarkers and diagnostic modeling in the human IBD cohort. (A) Schematic representation of the clinical breath sampling cohort, comprising 118 patients with Inflammatory Bowel Disease (IBD) and 118 healthy controls (HCs). (B) Representative total ion current (TIC) chromatograms comparing the breath volatile organic compound (VOC) profiles between an IBD patient (red) and a healthy control (blue), highlighting distinct metabolic variations. (C) Performance ranking of seven machine learning algorithms based on the AUC in the test set. The Random Forest (RF) model demonstrated the highest diagnostic accuracy. (D) Receiver Operating Characteristic (ROC) curve of the optimized random forest model for distinguishing IBD patients from healthy controls. (E) Box plots illustrating the relative abundance of five identified key biomarkers (propanoic acid, butanoic acid, isobutyric acid, pentanoic acid, and 1,2-propanediol) in breath samples. Statistical significance was determined using the Mann–Whitney U test with Benjamini–Hochberg FDR correction ($p < 0.05$; FDR < 0.1). (F) Metabolic pathway analysis linking the identified short-chain fatty acids (SCFAs) and derivatives to gut microbial fermentation of dietary fibers/carbohydrates. (G) Conceptual framework illustrating the translational bottleneck in human studies (confounding factors and limited intervention) and the rationale for establishing a standardized mouse model platform to validate disease mechanisms and therapeutic responses.

from approximately 8.0 ng L^{-1} in the healthy group to about 4.0 ng L^{-1} in the disease group, a drop of nearly 50%. The decrease in isobutanoic acid was even more significant, with its concentration level reduced by about 55% (from ~1.5 ng L^{-1} to <0.7 ng L^{-1}). This systemic deficiency of SCFAs and their derivatives is generally attributed to severe dysbiosis of the gut microbiota, particularly the reduced abundance of acid-producing bacteria (*e.g.*, *Faecalibacterium* and *Eubacterium*). Multiple clinical studies and meta-analyses have also confirmed that SCFA levels in the gut and various biological samples (feces and blood) of IBD patients are significantly reduced. Furthermore, their concentrations are negatively correlated with intestinal inflammation activity.[29–31] Notably, our parallel analysis of concurrent urine samples also revealed a consistent downward trend for these biomarkers (SI Fig. S1). This further confirms their reliability as indicators of systemic metabolic disorder, rather than originating merely as local products from the oral cavity. This cross-matrix commonality of metabolic features also provides a solid basis for using breath as a non-invasive window for monitoring systemic metabolic status.[32,33] Metabolic pathway enrichment analysis suggested (Fig. 2F) that these substances primarily originate from the anaerobic fermentation of carbohydrates and dietary fibers by gut microbiota.[34,35] Their down-regulation in breath may reflect the reduced abundance and impaired function of acid-producing gut bacteria in the IBD state. Additionally, microbial fermentation derivatives like 1,2-propanediol have also been shown to be closely related to changes in gut microbial metabolism,[36] supporting our interpretation of it as a candidate biomarker for microbial metabolic alterations.

However, although the clinical study established a clear correlation of the down-regulation of SCFAs and their derivatives in IBD, it also exposed key methodological challenges. In a clinical environment with confounding factors such as complex diet and medication, it is difficult to precisely resolve the dynamic response of these biomarkers to therapeutic interventions. It is also impossible to directly validate their "gut–lung axis" transport mechanism at the *in vivo* level

(Fig. 2G). Therefore, to deeply investigate their generation, transport, and exhalation processes, it is necessary to rely on animal models with highly controlled environments. This limitation highlights the necessity of building a high-fidelity animal experiment platform. It also provides a clear research direction and strategy for using the FaunaScope system for full-cycle longitudinal monitoring to solve complex translational medicine problems.

3.3 Implementation of a standardized longitudinal monitoring protocol and confirmation of biological phenotypes

To evaluate the monitoring stability of the FaunaScope system under long-term, dynamic interference conditions, this study first established a longitudinal experimental cohort. It involved disease induction (DSS) and nutritional intervention (EEN) (Fig. 3A). This experiment aimed to validate if the platform could, during long-term, multi-time-point monitoring, accurately capture the metabolic trajectory deviation caused by acute inflammation and the phenotypic reversal brought by treatment. The experimental workflow included an adaptation period (Days 1–3) and a subsequent modeling-intervention period (Days 4–11). During this period, mice in the DSS group only ingested a 2% DSS solution and standard chow. The EEN group received exclusive enteral nutrition liquid to replace solid chow, simulating the clinical exclusive enteral nutrition therapy model (in animal models, EEN has been reported to alleviate DSS-induced inflammation and improve pathological indicators[37]). Therefore, this design is both clinically comparable and facilitates the evaluation of the FaunaScope's sensitivity to intervention responses under controlled conditions.

First, longitudinal tracking of systemic clinical indicators revealed significant inter-group differences. Body weight monitoring showed (Fig. 3B) that mice in the DSS model group experienced a sharp weight loss (down to 75% of baseline) in the late modeling stage (Days 9–11), presenting a typical cachectic state. This wasting phenotype is consistent with severe diarrhea, dehydration, and enhanced systemic protein catabolism caused by acute colitis.[38] In contrast, the body weight of the EEN intervention group significantly rebounded

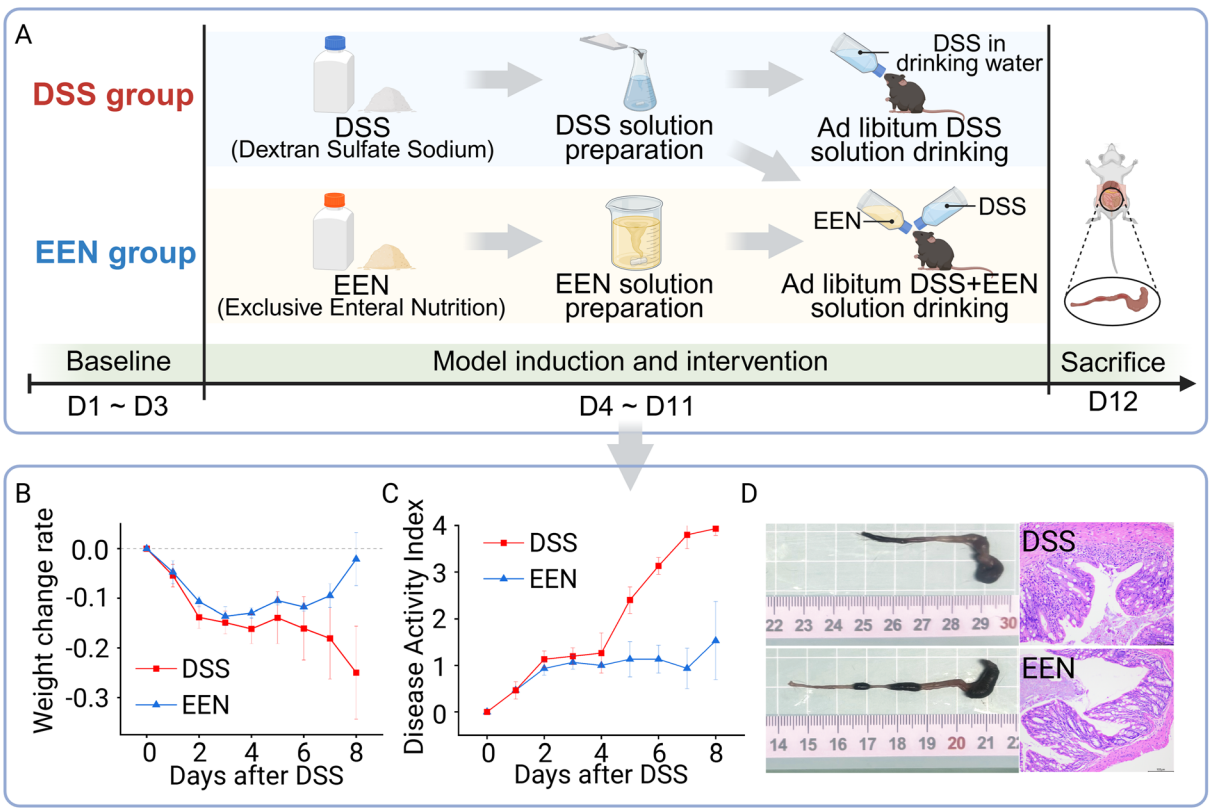

Fig. 3 Experimental design and phenotypic validation of the IBD mouse model under EEN intervention. (A) Schematic workflow of the animal study. Following a 3-day habituation period, C57BL/6 mice were randomized into two groups (n = 6/group) and subjected to an 8-day Dextran Sulfate Sodium (DSS) challenge. The DSS group received a standard diet, while the EEN group was exclusively fed with Exclusive Enteral Nutrition (EEN) solution to mimic clinical therapy. (B) Percentage body weight change relative to baseline (Day 4) across the experimental timeline. Data are presented as mean ± SEM. (C) Disease Activity Index (DAI) scores monitoring the clinical severity of colitis, calculated based on weight loss, stool consistency, and gross bleeding. The EEN group showed significantly alleviated symptoms compared to the DSS group. (D) Macroscopic and microscopic assessment of colonic damage. Left panel: representative images of explanted colons, showing significant shortening and hyperemia in the DSS group, which were ameliorated by EEN intervention. Right panel: representative H&E-stained colonic sections (200× magnification). The DSS group exhibited severe crypt distortion, epithelial erosion, and inflammatory infiltration (indicated by arrows), whereas the EEN group retained relatively intact mucosal architecture.

and approached the baseline (>98%) at the experimental endpoint. This confirmed the effectiveness of exclusive enteral nutrition in counteracting inflammation-related energy deficit.[39,40] The DAI score further quantified this phenotypic difference (Fig. 3C): the DAI score of the DSS group progressively worsened over time, reaching a peak on Day 11 (score near 4.0). In contrast, the DAI curve of the EEN group remained at a low level throughout (<2.0, $p < 0.05$), visually reflecting the excellent efficacy of EEN in alleviating clinical symptoms.

In the anatomical and histopathological evaluations at the experimental endpoint, we observed macroscopic and microscopic pathological changes that were highly consistent with the clinical phenotype. Gross morphology showed that the colons of mice in the DSS group exhibited extremely significant shortening (approx. 30% shorter than those of the EEN group) (Fig. 3D and SI S2A). This was due to smooth muscle spasm and fibrosis caused by transmural inflammation.[41] At the microscopic level, the H&E staining results (Fig. 3D) further revealed the injury mechanism: sections from the model group showed extensive disintegration of the crypt structure, depletion of goblet cells, and massive inflammatory cell infiltration in the mucosa and submucosa. These are all typical pathological features of DSS-induced colon injury.[42] Conversely, in the EEN intervention group, the aforementioned pathological changes were significantly suppressed. The colon length remained normal, and relatively intact crypt architecture and epithelial continuity were visible under the microscope, indicating that EEN can effectively promote mucosal healing.[39] Quantitative analysis of the histological score also reconfirmed that EEN intervention could reduce the intestinal microscopic pathological damage score by 45% (SI Fig. S2B).

In summary, the systemic clinical, anatomical, and histopathological data all confirmed that this study successfully constructed a severe IBD mouse model and an effective EEN intervention model. This laid a reliable biological foundation for subsequent in-depth breath metabolomics analysis based on the FaunaScope system.

3.4 Establishment of a dynamic quality control strategy for complex biological matrix interference

During the long-term longitudinal breath monitoring of IBD model mice, we noted that unavoidable excretion behaviors (defecation or urination) within the restrainer constituted the main source of random interference. Previous studies have indicated that feces and urine are some of the important release sources of *in vivo* VOCs. The volatiles from these matrices have significant overlap with breath VOCs. If not controlled, they become strong background interference for breath analysis, severely affecting the data's signal-to-noise ratio and interpretability.[43] Based on this, this study defined samples with recorded excretion events during sampling as the WE group (With Excretion events) and samples without any excretion behavior as the NE group (No Excretion events). A systematic comparative analysis was then conducted (Fig. 4).

PCA intuitively revealed the drastic perturbation of excretion behavior on breath fingerprints (Fig. 4A). Under the three physiological backgrounds of healthy (HC), model (DSS), and intervention (EEN), the WE group samples all significantly deviated from their corresponding NE group cluster centers. Their intra-group dispersion also increased substantially. This indicates that VOCs released from excreta constitute strong background noise sufficient to mask endogenous metabolic features. Bubble plot analysis further confirmed the broad-spectrum nature of this interference. In the WE group, over 80% of the detected compounds showed a "large circle/dark red" feature, representing high concentrations. This displayed an explosive signal enhancement across the full spectrum (Fig. 4B). This is attributed to the release of large amounts of highly volatile compounds from fresh excreta under the effects of body temperature and airflow.

To identify universal "excretion event indicators," we performed differential screening between WE and NE within all three experimental groups ($p < 0.05$). A network Venn diagram was used to extract the intersection (Fig. 4C). The results showed that although there were subtle differences in the excretion metabolite profiles at different physiological states, ethyl acetate and dimethyl sulfide were consistently identified as core intersecting substances. This finding is of great significance. It indicates that these two substances are stable excretion markers unaffected by the disease state. The violin plot (Fig. 4D) further revealed their astonishing interference intensity. Compared to the NE group, the mean concentration of dimethyl sulfide in WE group samples increased by 2–3 times, while ethyl acetate surged by 5–10 times. From a biochemical mechanism perspective, dimethyl sulfide is a typical metabolic end-product from the degradation of sulfur-containing amino acids (*e.g.*, methionine) by gut anaerobic bacteria. Its high abundance in fecal headspace has been confirmed by research to be a direct indicator of gut microbial fermentation activity.[44,45] Ethyl acetate, as a downstream product of ethanol and acetic acid under the action of microbial esterases, is also widely present in biological excreta.[46,47] Therefore, these two compounds can serve as reliable "characteristic interfering substances" to identify potential sample contamination or background interference in animal experimental breath analysis. While ethyl acetate and dimethyl sulfide serve as robust markers for excretion interference in our current model, their universality requires further investigation. Because the production of these volatile metabolites is closely linked to gut microbiota and host metabolism, their baseline levels may vary across different mouse strains, diverse dietary interventions (beyond EEN), or specific disease models with severe dysbiosis. Therefore, validating the stability of these markers—or identifying context-specific alternatives—across broader biological conditions represents an important direction for future research to standardize this QC strategy.

Based on the above findings, this study established a quality control strategy based on monitoring excretion behavior. That is, during the data filtering stage, if an excretion event was observed and recorded for a sample during sampling, or if an abnormal synergistic increase in the concentrations of ethyl acetate and dimethyl sulfide was found during data post-processing, then that sample is defined as a contaminated

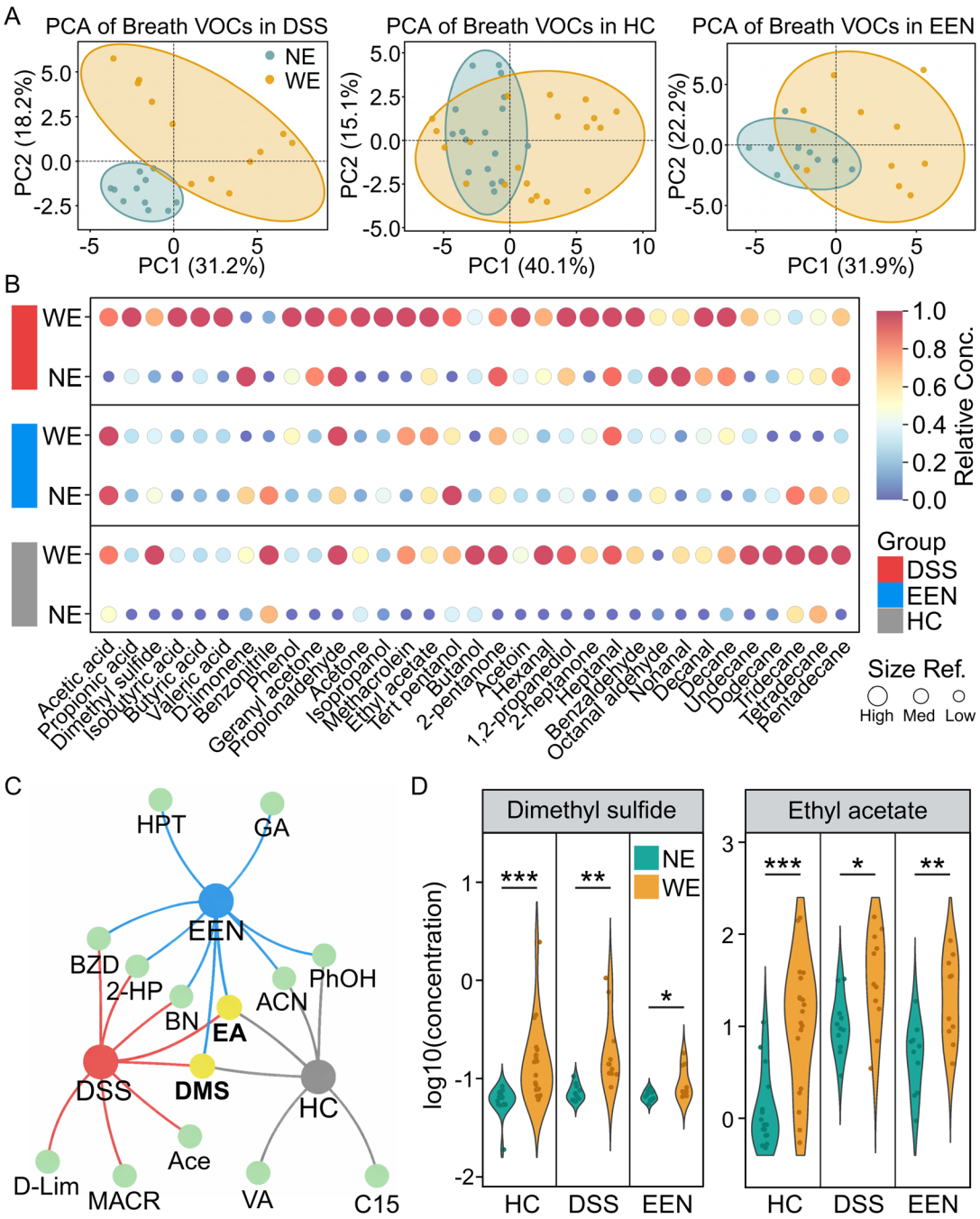

Fig. 4 Identification of excretion-associated interference and establishment of a data cleaning strategy. (A) Principal Component Analysis (PCA) score plots demonstrating the distinct separation between samples with excretion events (WE, red) and samples with no excretion events (NE, green) across HC, DSS, and EEN groups. The segregation indicates a systematic metabolic shift caused by excretion. (B) Bubble plot visualization of the abundance profiles of all detected VOCs. The color and size of each dot represent the mean relative concentration of the compound within the group (redder and larger dots indicate higher concentrations). WE samples exhibit a globally elevated intensity pattern among these compounds compared to NE samples, reflecting complex matrix effects from excretion. (C) Network Venn diagram illustrating the intersection of significantly differential VOCs (WE *vs.* NE; $p < 0.05$) identified independently within HC, DSS, and EEN groups. Ethyl acetate and dimethyl sulfide were identified as common intersection compounds. (D) Violin plots showing the relative abundance of the two identified core interference markers (ethyl acetate and dimethyl sulfide). These compounds show consistent and dramatic abundance spikes in WE samples across all experimental conditions, serving as chemical indicators of excretion contamination.

sample and is excluded from subsequent analysis. This quality control strategy fills a methodological blind spot in existing rodent breath research, which often overlooks matrix background interference. Although this strategy sacrifices some sample size, it effectively eliminates exogenous interference. This ensures that the final retained data can truly reflect the

endogenous metabolic changes exhaled from the lungs of mice. This is not only an important component of the SOP for the cross-species breath analysis platform but also lays a solid data quality foundation for the subsequent precise analysis of faint endogenous metabolic signals and cross-species heterogeneity under an interference-free background.

3.5 Discovery of cross-species metabolic heterogeneity and validation of the platform's mechanistic elucidation capabilities

Thanks to the aforementioned strict quality control strategy, we were able to conduct an in-depth analysis of the interference-free breath metabolic profiles of the HC, DSS, and EEN groups of mice. Although the full-spectrum heatmap analysis showed that DSS modeling caused extensive systemic metabolic perturbations (see SI Fig. S3 for details), this study focused on a targeted analysis of SCFAs and their derivatives (propanoic acid, butanoic acid, isobutanoic acid, and 1,2-propanediol). This was done considering the translational correspondence and biological specificity, as these compounds highly overlap with human IBD breath features.

The expression profile of key biomarkers (Fig. 5A) intuitively displayed significant inter-group differences. The DSS model group showed a consistent high-expression feature compared to the HC. The quantitative violin plot (Fig. 5B) further revealed the drastic extent of this change. Specifically, except for isobutanoic acid, the mean signal intensities of propanoic acid, butanoic acid, and 1,2-propanediol in the DSS group were significantly elevated by about 2–3 times compared to the HC group ($p < 0.05$).

Notably, we observed an interesting phenomenon. The levels of all four biomarkers in the EEN intervention group not only

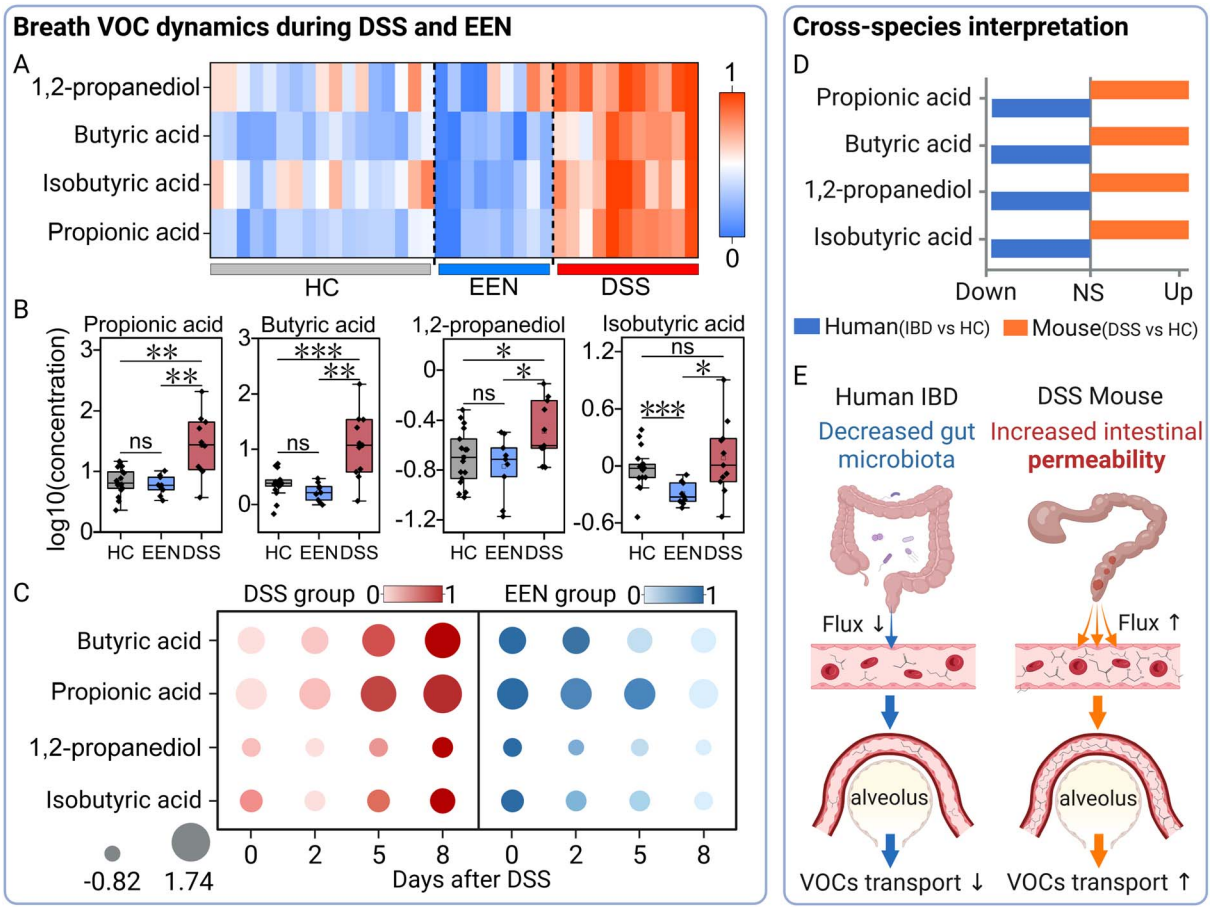

Fig. 5 Volatilomic profiling of IBD mice and translational mechanism insight. (A) Targeted heatmap of key biomarker expression profiles (propanoic acid, butanoic acid, isobutyric acid, 1,2-propanediol). The DSS group exhibits a distinct upregulation pattern (red), whereas the EEN group shows a downregulation trend (blue). (B) Violin plots quantifying the relative abundance of the four biomarkers ($n = 6$/group). While the DSS group shows significantly elevated levels compared to HC/EEN, the EEN group exhibits levels lower than or comparable to those of HCs, attributed to EEN-induced microbiota remodeling. (*: $p < 0.05$; **: $p < 0.01$). (C) Temporal bubble heatmap illustrating the dynamic changes of biomarkers on Days 4, 8, and 11. Bubble size represents log-transformed concentration, and color intensity indicates relative variation (0–1 scale). The DSS group shows a progressive increase in abundance over time, whereas the EEN group maintains low levels. (D) Cross-species comparison revealing a divergent trend: breath SCFAs are downregulated in human IBD patients but upregulated in DSS mice. (E) Schematic mechanism explaining the divergence. Human IBD (chronic): dysbiosis leads to reduced SCFA production and lower breath levels. Mouse IBD (acute): severe epithelial barrier disruption (leaky gut) facilitates the passive influx of luminal SCFAs into the bloodstream, causing elevated breath levels despite potential dysbiosis.

significantly decreased ($p < 0.05$ *vs.* DSS) but were also generally lower in value than the HC group baseline. The decrease in isobutanoic acid was particularly significant (approx. 50% of the baseline level). This phenomenon can be attributed to the specific remodeling effect of EEN intervention on the gut microbiota. Previous studies have pointed out that exclusive enteral nutrition, as a monotonous diet, can not only effectively control inflammation but also lead to a decrease in microbial diversity and total biomass due to substrate uniformity.[48] Therefore, the overall decline of SCFA levels in the breath of the EEN group is likely a direct reflection of the absolute reduction in fermentation capacity of the gut's acid-producing bacteria under special dietary pressure.

To capture the dynamic trajectory of these metabolic changes, we plotted a time-series bubble heatmap during the modeling period (Fig. 5C). The results showed that the bubble volume of the DSS group increased linearly over time (Days 5, 8, and 11), reaching a peak in the late modeling stage (Day 11). This indicates that the exhalation of metabolites was highly positively correlated with inflammation progression. Conversely, the bubbles of the EEN group remained consistently small, confirming that the nutritional intervention continuously suppressed the occurrence of metabolic disorders throughout the entire treatment window.

However, when we compared the mouse data with the clinical cohort results in a cross-species manner, we observed a significant divergence in the human-mouse breath metabolic features. Specifically, under the same IBD pathological background, SCFAs in the breath of human patients were generally decreased compared to healthy humans. In contrast, breath SCFAs in DSS mice showed a consistent increase compared to healthy mice (Fig. 5D).

Regarding this seemingly contradictory phenomenon, this study, by combining the pathological characteristics of the DSS model with previous mechanistic research, for the first time constructed a differential mechanism model of "acute leakage *vs.* chronic dysbiosis" (Fig. 5E). On one hand, the core pathology of DSS-induced colitis is an acute inflammation characterized by chemical epithelial denudation and barrier collapse.[49] We infer that under this extreme condition, although the gut microbiota may have already shown initial dysbiosis, the complete failure of the physical barrier becomes the dominant factor. This leads to the high concentration of SCFAs, originally accumulated in the intestinal lumen, losing the mucosal barrier's obstruction. They can then passively and unimpededly leak into the blood circulation through the severely damaged epithelium, ultimately triggering an abnormal increase in the signal at the breath end. On the other hand, clinical IBD is usually in a long-term chronic inflammatory process. Multiple metagenomic studies have confirmed that its core feature is the abundance depletion and functional loss of acid-producing bacteria (*e.g.*, *Faecalibacterium prausnitzii*).[50,51] At this time, although there is also increased intestinal permeability in patients, the deficiency in source generation capacity becomes dominant. This results in SCFAs manifesting as a metabolic decrease in the breath.

This profound mechanistic insight strongly demonstrates the core value of the breath analysis platform constructed in this study. It not only possesses the high sensitivity to capture subtle metabolic fluctuations, but more importantly, through systematic longitudinal monitoring in controlled animal experiments, the platform successfully elucidated complex pathophysiological mechanisms that are inaccessible by relying solely on clinical correlation studies. This confirms that our platform is not just a high-precision analytical tool, but also a powerful mechanism-elucidation platform. It can provide key evidence for connecting clinical phenotypes with basic pathology and for revealing the complex interactions between them.

Finally, a limitation of this study is the relatively small sample size ($n = 6$ per group), which was chosen in adherence to the 'reduction' principle of animal ethics for this exploratory research. Given the inherently high inter-individual biological variability in breath VOC profiles, this sample size limits the statistical power for robust biomarker validation. Future studies involving larger animal cohorts are warranted to comprehensively validate these initial findings.

4 Conclusions

This study constructed and systematically validated a cross-species breath metabolomics analysis platform. It was designed to address key methodological problems in translational breath research, particularly those concerning the sample collection process and insufficient data comparability. By integrating a rigorous clinical breath sampling protocol, a self-designed breath collection system for small laboratory animals (FaunaScope), and TD-GC-MS/MS analysis, a universal analytical workflow for both human and mouse models was established. The methodological evaluation results showed that the platform performed well in detection sensitivity for low-abundance volatile organic compounds, analytical repeatability, and temporal stability. Concurrently, this study proposed and implemented a quality control strategy for contamination related to excretion events. It was confirmed that ethyl acetate and dimethyl sulfide can serve as stable characteristic interfering substances for excretion. These are used to identify and exclude contaminated breath samples, thereby significantly enhancing the data reliability for longitudinal monitoring and cross-species comparative analysis. The application results of this platform to IBD patients and DSS-induced colitis mouse models showed that acute barrier disruption and chronic gut dysbiosis can present different patterns in breath metabolic features. This suggests that when interpreting breath VOC signals, their generation, transport, and exhalation processes must be comprehensively considered. Overall, this study provides a generalizable analytical framework for cross-species breath metabolomics research and lays a methodological foundation for subsequent mechanistic studies and translational applications.

Author contributions

Zhiheng Yu: conceptualization, methodology, investigation, data curation, formal analysis, visualization, writing original draft; Yongyan Ji: methodology, investigation; Zijun Meng: resources, validation; Xiang Li: supervision, funding acquisition, writing – review and editing. All authors reviewed and approved the manuscript.

Conflicts of interest

The authors declare that they have no known competing financial interests or personal relationships that could have appeared to influence the work reported in this paper.

Data availability

The processed breath VOC concentration datasets supporting this study are publicly available at GitHub (https://github.com/yuzhihuan/data). The repository includes both human and mouse breath VOC data. All datasets have been fully anonymized, and no personally identifiable information is included.

Supplementary information (SI): additional experimental details, supplementary texts, tables, and figures. See DOI: https://doi.org/10.1039/d6ay00164e.

Acknowledgements

This work was supported by the National Natural Science Foundation of China (No. 22476023 and No. 22276038), AI for Science Foundation of Fudan University (No. FudanX24AI026), Agilent Research Gift (No. 4956), and Wuxi Industrial Innovation Research Institute (Proof-of-Concept Project No. ZK202506034-SY-01[A]).

References

1 P. Wang, Q. Huang, S. Meng, T. Mu, Z. Liu, M. He, Q. Li, S. Zhao, S. Wang and M. Qiu, *Eclinicalmedicine*, 2022, **47**, 101384.
2 Y. Liu, Y. Ji, J. Chen, Y. Zhang, X. Li and X. Li, *Theranostics*, 2024, **14**, 4240–4255.
3 G. Purcaro, M. Nasir, F. Franchina, C. Rees, M. Aliyeva, N. Daphtary, M. Wargo, L. Lundblad and J. Hill, *Metabolomics*, 2019, **15**, 10.
4 F. Franchina, T. Mellors, M. Aliyeva, J. Wagner, N. Daphtary, L. Lundblad, S. Fortune, E. Rubin and J. Hill, *J. Breath Res.*, 2018, **12**, 026008.
5 K. Hintzen, M. Eussen, C. Neutel, N. Bouvy, F. van Schooten, C. Hooijmans and T. Lubbers, *PLoS One*, 2023, **18**, e0291636.
6 O. Lawal, W. Ahmed, T. Nijsen, R. Goodacre and S. Fowler, *Metabolomics*, 2017, **13**, 110.
7 Y. He, Z. Su, T. Sha, X. Yu, H. Guo, Y. Tao, L. Liao, Y. Zhang, G. Lu, G. Lu and W. Gong, *J. Thorac. Dis.*, 2024, **16**, 7978–7998.
8 K. Westphal, D. Dudzik, M. Waszczuk-Jankowska, B. Graff, K. Narkiewicz and M. Markuszewski, *Metabolites*, 2023, **13**, 8.
9 Q. Li, X. Fu, K. Xu, H. He and N. Jiang, *Microchem. J.*, 2021, **160**, 105611.
10 J. Zhu, H. Bean, J. Jiménez-Díaz and J. Hill, *J. Appl. Physiol.*, 2013, **114**, 1544–1549.
11 S. Ghosh, K. Kim and J. Sohn, *Thescientificworldjournal*, 2011, **11**, 2160–2177.
12 P. Mochalski, J. King, K. Unterkofler and A. Amann, *Analyst*, 2013, **138**, 1405–1418.
13 R. Remy, N. Kemnitz, P. Trefz, P. Fuchs, J. Bartels, A. Klemenz, L. Rührmund, P. Sukul, W. Miekisch and J. Schubert, *Iscience*, 2022, **25**, 105195.
14 D. Smith and P. Spanel, *Mass Spectrom. Rev.*, 2005, **24**, 661–700.
15 T. Bruderer, T. Gaisl, M. Gaugg, N. Nowak, B. Streckenbach, S. Müller, A. Moeller, M. Kohler and R. Zenobi, *Chem. Rev.*, 2019, **119**, 10803–10828.
16 Y. Yan, Q. Wang, W. Li, Z. Zhao, X. Yuan, Y. Huang and Y. Duan, *RSC Adv.*, 2014, **4**, 25430–25439.
17 M. Lombardi, A. Segreti, M. Miglionico, G. Pennazza, L. Tocca, L. Amendola, R. Vergallo, G. Di Sciascio, I. Porto, F. Grigioni and R. Incalzi, *J. Clin. Med.*, 2024, **13**, 5857.
18 W. Arulvasan, H. Chou, J. Greenwood, M. Ball, O. Birch, S. Coplowe, P. Gordon, A. Ratiu, E. Lam, A. Hatch, M. Szkatulska, S. Levett, E. Mead, C. Charlton-Peel, L. Nicholson-Scott, S. Swann, F. van Schooten, B. Boyle and M. Allsworth, *Metabolomics*, 2024, **20**, 102.
19 M. Bajo-Fernández, E. Souza-Silva, C. Barbas, M. Rey-Stolle and A. García, *Front. Mol. Biosci.*, 2024, **10**, 1295955.
20 A. Taylor, S. Blum, M. Ball, L. Pocock, O. Birch, H. Chou, J. Greenwood, S. Swann, E. Crone, B. Boyle, M. Allsworth and K. Geillinger-Kästle, *Eur. Respir. J.*, 2024, **64**, PA1714.
21 K. Hintzen, A. Smolinska, A. Mommers, N. Bouvy, F. van Schooten and T. Lubbers, *J. Breath Res.*, 2022, **16**, 027102.
22 A. Verma, T. Bhagchandani, A. Rai, U. Sardarni, N. Bhavesh, S. Gulati, R. Malik and R. Tandon, *ACS Omega*, 2024, **9**, 14648–14671.
23 S. Li, Z. Yu, Z. Cen and X. Li, *Green Anal. Chem.*, 2025, **14**, 100284.
24 Y. Ji, Z. Yu, Y. Huang, W. Wang, M. Cao and X. Li, *ACS Sens.*, 2025, **11**, 224–236.
25 J. Kwak, M. Fan, J. A. Martin, D. K. Ott and C. C. Grigsby, *Anal. Sci.*, 2017, **33**, 147–152.
26 S. Kurada, N. Alkhouri, C. Fiocchi, R. Dweik and F. Rieder, *Aliment. Pharmacol. Ther.*, 2015, **41**, 329–341.
27 X. Zhang, Y. Han, J. Zhang and Y. Duan, *Gut*, 2022, **71**, A137–A139.
28 H. Yang, Y. Wang, H. Peng and C. Huang, *Sci. Rep.*, 2021, **11**, 103.
29 L. Chulenbayeva, Z. Jarmukhanov, K. Kaliyekova, S. Kozhakhmetov and A. Kushugulova, *Biomolecules*, 2025, **15**, 1017.
30 H. Zhao, Y. Zhou, J. Xu, Y. Zhang, H. Wang, C. Zhao, H. Huang, J. Yang, C. Huang, Y. Li, L. Wang and Y. Nie, *J. Transl. Med.*, 2024, **22**, 369.

31 G. Lo Sasso, L. Khachatryan, A. Kondylis, J. Battey, N. Sierro, N. Danilova, T. Grigoryeva, M. Markelova, D. Khusnutdinova, A. Laikov, I. Salafutdinov, Y. Romanova, M. Siniagina, I. Vasiliev, E. Boulygina, V. Solovyeva, E. Garanina, K. Kitaeva, K. Ivanov, D. Chulpanova, K. Kletenkov, A. Valeeva, A. Odintsova, M. Ardatskaya, R. Abdulkhakov, N. Ivanov, M. Peitsch, J. Hoeng and S. Abdulkhakov, *Inflamm. Bowel Dis.*, 2021, **27**, 418–433.
32 L. Ning, Y. Zhou, H. Sun, Y. Zhang, C. Shen, Z. Wang, B. Xuan, Y. Zhao, Y. Ma, Y. Yan, T. Tong, X. Huang, M. Hu, X. Zhu, J. Ding, Y. Zhang, Z. Cui, J. Fang, H. Chen and J. Hong, *Nat. Commun.*, 2023, **14**, 7135.
33 K. Gallagher, A. Catesson, J. Griffin, E. Holmes and H. Williams, *J. Crohns Colitis*, 2021, **15**, 813–826.
34 P. Cronin, S. Joyce, P. O'Toole and E. O'Connor, *Nutrients*, 2021, **13**, 1655.
35 M. Yuan, K. Gao, K. Peng, S. Bi, X. Cui and Y. Liu, *Foods*, 2025, **14**, 3649.
36 F. Faber, P. Thiennimitr, L. Spiga, M. Byndloss, Y. Litvak, S. Lawhon, H. Andrews-Polymenis, S. Winter and A. Bäumler, *PLoS Pathog.*, 2017, **13**, e1006129.
37 T. Yu, Q. Yu, X. Chen, L. Zhou, Y. Wang and C. Yu, *Int. J. Mol. Med.*, 2018, **42**, 1305–1316.
38 S. Wirtz, C. Neufert, B. Weigmann and M. Neurath, *Nat. Protoc.*, 2007, **2**, 541–546.
39 G. Lunken, K. Tsai, A. Schick, D. Lisko, L. Cook, B. Vallance and K. Jacobson, Cellular and Molecular, *Gastroenterol. Hepatol.*, 2021, **12**, 1251–1266.
40 G. Li, X. Wu, X. Gao, R. Lin, L. Chen, M. Sun, J. Jia, Z. Liu, L. Fang and W. Wu, *Food Funct.*, 2022, **13**, 1725–1740.
41 Y. Yan, V. Kolachala, G. Dalmasso, H. Nguyen, H. Laroui, S. Sitaraman and D. Merlin, *PLoS One*, 2009, **4**, e6073.
42 X. Xu, S. Lin, Y. Yang, X. Gong, J. Tong, K. Li and Y. Li, *Exp. Ther. Med.*, 2020, **20**, 1987–1994.
43 P. Moura, M. Raposo and V. Vassilenko, *Biomed. J.*, 2023, **46**, 100623.
44 K. Sakuma, S. Hayashi, Y. Yasaka, H. Nishijima, H. Funabashi, M. Hayashi, H. Matsuoka and M. Saito, *Exp. Anim.*, 2013, **62**, 101–107.
45 C. Garner, S. Smith, B. Costello, P. White, R. Spencer, C. Probert and N. Ratcliffe, *FASEB J.*, 2007, **21**, 1675–1688.
46 C. Yao, K. Green, A. Day, Z. Ardalan, R. Slater, R. Bryant, P. Gibson and C. Probert, *Mol. Nutr. Food Res.*, 2025, **69**, e70003.
47 G. Riccio, S. Baroni, A. Urbani and V. Greco, *Metabolites*, 2022, **12**, 1072.
48 G. Li, X. Wu, X. Gao, R. Lin, L. Chen, M. Sun, J. Jia, Z. Liu, L. Fang and W. Wu, *Food Funct.*, 2022, **13**, 1725–1740.
49 B. Chassaing, J. D. Aitken, M. Malleshappa and M. Vijay-Kumar, *Curr. Protoc. Immunol.*, 2014, **104**, 15251–152514.
50 J. Lloyd-Price, C. Arze, A. Ananthakrishnan, M. Schirmer, J. Avila-Pacheco, T. Poon, E. Andrews, N. Ajami, K. Bonham, C. Brislawn, D. Casero, H. Courtney, A. Gonzalez, T. Graeber, A. Hall, K. Lake, C. Landers, H. Mallick, D. Plichta, M. Prasad, G. Rahnavard, J. Sauk, D. Shungin, Y. Vázquez-Baeza, R. White, J. Braun, L. Denson, J. Jansson, R. Knight, S. Kugathasan, D. McGovern, J. Petrosino, T. Stappenbeck, H. Winter, C. Clish, E. Franzosa, H. Vlamakis, R. Xavier, C. Huttenhower, J. Bishai, K. Bullock, A. Deik, C. Dennis, J. Kaplan, H. Khalili, L. McIver, C. Moran, L. Nguyen, K. Pierce, R. Schwager, A. Sirota-Madi, B. Stevens, W. Tan, J. ten Hoeve, G. Weingart, R. Wilson, V. Yajnik and I. Investigators, *Nature*, 2019, **569**, 655.
51 Y. Cao, J. Shen and Z. Ran, *Gastroenterol. Res. Pract.*, 2014, **2014**, 872725.